

NASA TECHNICAL NOTE



NASA TN D-5052

2.1

NASA TN D-5052



LOAN COPY: RETURN TO
AFWL (WLIL-2)
KIRTLAND AFB, N MEX

COMPUTATION OF TOPSIDE IONOGRAMS FROM $N(h)$ PROFILES

by

Lawrence Colin and Kwok-Long Chan
Ames Research Center

and

Jack G. K. Lee
Informatics, Inc.



0131947

COMPUTATION OF TOPSIDE IONOGRAMS FROM $N(h)$ PROFILES

By Lawrence Colin and Kwok-Long Chan

Ames Research Center
Moffett Field, Calif.

and

Jack G. K. Lee

Informatics, Inc.
Palo Alto, Calif.

NATIONAL AERONAUTICS AND SPACE ADMINISTRATION

For sale by the Clearinghouse for Federal Scientific and Technical Information
Springfield, Virginia 22151 - CFSTI price \$3.00

COMPUTATION OF TOPSIDE IONOGRAMS FROM $N(h)$ PROFILES

By Lawrence Colin and Kwok-Long Chan

Ames Research Center

and

Jack G. K. Lee

Informatics, Inc.

SUMMARY

Model profiles of plasma frequency and gyrofrequency are chosen to simulate typical conditions observed in the topside ionosphere by the Alouette I sounder (1000 km) and the Alouette II sounder near apogee (3000 km). Examples of group refractive index profiles for these models are presented. By means of parabolic-in-log X lamination techniques applied to the plasma frequency profiles, "cumulative delays" are computed to illustrate the relative delays contributed by each lamination to the formation of topside ionograms. Complete ionograms (ordinary, extraordinary, and Z traces) are presented for all the models. Implications of the results to the inverse experimental problem of scaling ionogram data and computing electron concentration profiles are discussed.

INTRODUCTION

Whereas research concerned with ionospheric sounding from the earth's surface is more than 25 years old, sounding of the topside ionosphere from satellite-borne radars has been conducted for only six years. The satellites Alouette I (1962 to present, circular orbit at about 1000 km) and Alouette II (1965 to present, elliptical orbit with apogee at 3000 km, perigee at 500 km), containing HF swept-frequency sounders, have provided the bulk of available data on electron concentration, $N(h)$, above the F_2 layer peak.

Because of the complexities of topside ionograms, sophisticated $N(h)$ reduction procedures and programs have been developed. The standard reduction procedure involves computing the $N(h)$ profile from a set of virtual depth-frequency pairs, $h'(f)$, scaled from the extraordinary trace appearing on a filmed ionogram. This technique is adequate for the accurate reduction of the great bulk of Alouette I and low-altitude Alouette II ionograms (ref. 1). On the other hand, there remain a great number of topside ionograms, particularly those collected at the higher orbital altitudes of Alouette II, for which the standard reduction procedure yields inaccurate, often unrealistic, electron concentration profiles. The difficulties are caused mainly by scaling uncertainties associated with large virtual depths, $h'(f)$, steep gradients,

dh'/df , sharp "cusps," d^2h'/df^2 , and the occurrence of reflection traces arising from oblique propagation. Clearly, new procedures involving optimum use of independent and/or redundant information available in the ionogram data must be brought to bear if reliable high-altitude $N(h)$ profiles are to be computed. For example, the use of the redundant information available in all reflection traces may well enhance the accuracy of computed profiles.

The present study deals with the computation of ionograms from model $N(h)$ profiles. This direct approach clearly demonstrates the transformation performed by the ionosphere on the sounder waves and the one-to-one correspondence of true and virtual reflection heights (ref. 2). The results supply insight to the redundancy problem and suggest some feasible schemes for optimum implementation of $N(h)$ reduction procedures using extraordinary, ordinary, and Z trace data.

REFRACTIVE INDICES IN THE TOPSIDE IONOSPHERE

The transformation is described by

$$h'(f) = \int_{h_s}^{h_r(f)} \mu' dh \quad (1)$$

which relates the virtual depth, h' , of reflection of a particular propagation mode at a sounder frequency, f , to the true height of reflection, h_r , for a given profile of group refractive index, μ' , between the altitude of the satellite, h_s , and h_r . Appendix A details the appropriate group refractive index and phase refractive index, μ , equations expressed in terms of the familiar magnetoionic parameters X , Y , and θ . Before proceeding with the major purpose, it is instructive to examine carefully the variations of μ and μ' with these parameters.

The variation of μ^2 and μ' with X is illustrated in figure 1 for a value of $Y < 1$ and in figure 2 for a value of $Y > 1$. Curves are shown for several values of θ . A combination of linear and reciprocal scales is used to include both zero and infinity on abscissa and ordinate. For $Y < 1$ (fig. 1) there is one branch for the ordinary mode ($0 \leq X \leq 1$) and two branches for the extraordinary mode ($0 \leq X \leq 1 - Y$ and $(1 - Y^2)/(1 - Y^2 \cos^2 \theta) \leq X \leq 1 + Y$). The latter branch of the extraordinary mode is referred to as the Z mode. For $Y > 1$ (fig. 2) the ordinary mode has two branches ($0 \leq X \leq 1$ and $(1 - Y^2)/(1 - Y^2 \cos^2 \theta) \leq X$; the latter branch is called the whistler mode and exists only when $Y^2 \cos^2 \theta > 1$) while the extraordinary mode has only one branch, the Z mode branch ($0 \leq X \leq 1 + Y$). The ordinary, extraordinary, and Z modes are consistently observed as distinct reflection traces in topside ionograms. Nonzero values of X at the satellite sounder antennas allow the observation of the Z mode for $Y < 1$. In bottomside ionograms the Z trace is observed for $Y < 1$ only when wave coupling exists between the ordinary and extraordinary modes (ref. 3).

Zeros in μ^2 occurring at $X = 1$ (ordinary mode), $X = 1 - Y$ (extraordinary mode), and $X = 1 + Y$ (Z mode) correspond to wave reflection conditions for the respective modes. An infinity in μ^2 occurs at $X = (1 - Y^2)/(1 - Y^2 \cos^2 \theta)$ (Z mode for $Y < 1$, and ordinary mode for $Y > 1$). Clearly, both zeros and infinities in μ^2 correspond to infinities in μ' . However, the infinity in μ' associated with $X = (1 - Y^2)/(1 - Y^2 \cos^2 \theta)$ is not a wave reflection condition as are the other infinities.

Graphs of μ^2 and μ' similar to figures 1 and 2 have been published in references 3-6. In topside $N(h)$ reduction, it is necessary to take into account the Y variation with height. Thus it is useful to consider the variation of μ^2 and μ' with X and Y for a fixed value of θ , since θ is nearly independent of height for vertical propagation. Figures 3 and 4 illustrate the variations of μ^2 and μ' versus X for $\theta = 5^\circ$ and 55° , respectively, and for several values of Y for each propagation mode. These particular cases of θ are used in the analyses reported below. NASA TM X-1553 (ref. 7) contains many graphs of the types illustrated in figures 1 to 4.

TOPSIDE MODELS

Common types of ionograms observable from the Alouette sounders have been computed from equation (1) using several realistic model profiles of plasma frequency, $f_n(h)$, and gyrofrequency, $f_h(h)$, shown in figure 5. High and low $f_n(h)$ models and high and low $f_h(h)$ models extend from $h = 3000$ km to 400 km. The two $f_n(h)$ models have identical shapes corresponding to a theoretical plasma distribution based on vertical diffusive equilibrium such that the electron concentrations at any altitude differ by a factor of 5 between models (ref. 1). The high and low $f_h(h)$ models are dipolar (inverse cube) with magnitudes at 3000 km typical of those observed at high latitudes and low mid-latitudes, respectively. The propagation angles, θ , are independent of h with magnitudes 5° and 55° to simulate vertical propagation at high latitudes and low midlatitudes. A total of eight simulated Alouette cases, summarized in table I, were constructed from these models.

"CUMULATIVE DELAY" CURVES AND IONOGRAMS

For each case in table I, ionogram traces for each propagation mode may be calculated by integrating equation (1) using the group refractive index equations given in appendix A. The integration procedures are described in appendix B. The $f_n(h)$ and $f_h(h)$ profiles are subdivided into equal thickness contiguous laminations (100 km for cases 1 through 4, 40 km for cases 5 through 8). Within each lamination the height is assumed parabolic-in-log X (see appendix B) and f_h is assumed to vary in an inverse-cube manner. Using the reflection criteria described above, that is, ordinary mode ($X=1$), extraordinary mode ($X=1-Y$), and Z mode ($X=1+Y$), those frequencies reflected at the lower boundary of each lamination are calculated. These sets of

frequencies are used to compute the ionogram traces. Six examples are illustrated in figures 6 through 11. Part (a) of each figure shows the group refractive index profiles, $\mu'(h)$, appropriate to each lower boundary reflection frequency. The corresponding ionogram trace is given in part (b) where a smooth curve is drawn through the computed virtual delays for each reflection frequency. Also shown in part (b) are "cumulative delay" curves which illustrate the relative delays contributed by each lamination as the sounder wave "propagates" to the reflection level.

Figure 6 represents computation of the extraordinary mode for case 1. At each frequency, $\mu'(h)$ increases monotonically and smoothly from a finite value at the satellite to infinity at the altitude of reflection corresponding to the condition $X = 1 - Y$. Integration of the $\mu'(h)$ curves produces a moderate "cusp" in the extraordinary trace at frequencies slightly greater than the satellite cutoff frequency, f_{XS} . The "cumulative delay" curves quite closely parallel the trace, and the delay in the lowest lamination, for each frequency, is significantly greater than the delays in each of the preceding laminations. These variations are typical of extraordinary mode variations for all eight cases. Subtle differences do occur between the results of the high and low $f_h(h)$ models because the extraordinary mode group refractive index is sensitive to Y , but not to θ , as seen in figures 3 and 4.

Figures 7 and 8 represent two examples for the ordinary mode (cases 1 and 2) in which the $\mu'(h)$ profiles are quite similar to each other, that is, $\mu'(h)$ varies smoothly from finite values at the satellite to infinity at those altitudes where $X = 1$. However, the computed ionograms are quite dissimilar. Figure 7 illustrates the formation of a sharp "cusp" caused by an enormous delay encountered in the lamination of wave reflection which is typical for high-latitude ionograms where θ is small. Figure 8 illustrates the formation of a more moderate cusp. Although the delay in the last lamination is still largest relative to each of the preceding laminations, the absolute delay is considerably smaller than that in figure 7. The contrasts seen in figures 7 and 8 demonstrate that the ordinary mode group refractive index is a sensitive function of θ , but not of Y , as shown in figures 1 and 2.

The $\mu'(h)$ profiles and ionograms for the Z mode for cases 2, 4, and 8 are shown in figures 9, 10, and 11. Figure 9 shows that for low frequencies the variations of $\mu'(h)$ are similar to those in figures 6, 7, and 8. However, at higher frequencies ($f \geq 0.228$ Mc/s) a nonmonotonic behavior occurs when $\mu'(h)$ decreases with depth to a minimum value before increasing to infinity at the reflection level where $X = 1 + Y$. Finally, at a frequency, $f_{Z\infty}$, corresponding to $X = (1 - Y^2)/(1 - Y^2 \cos^2 \theta)$, μ' becomes infinite at the satellite and the Z mode ceases to propagate from the sounder antennas. This behavior is most frequently observed on topside Z traces. However, it is not unusual to encounter the situations shown in figures 10 and 11. Here, for low and medium frequencies, the $\mu'(h)$ profile behavior is quite similar to that described for figure 9. However, at frequencies ($f \geq 0.290$ Mc/s in fig. 10 and $f \geq 0.726$ Mc/s in fig. 11) close to $f_{Z\infty}$, the $\mu'(h)$ profiles take the peculiar variations shown, that is, $\mu'(h)$ exhibits two minimums and a maximum before increasing to infinity at the reflection level. This behavior is usually encountered for conditions of high $f_h(h)$ and low $f_n(h)$ where Y

is greater than 1 and X varies from less than to greater than 1. The well-defined maximums in figure 10 are due to the maximum of μ'_Z near $X = 1$ observed in figure 4(b) for values of Y near 2. The large values of $\mu'(h)$ immediately below the satellite height for $f = 0.959$ Mc/s in figure 11 are due to the large values of μ'_Z observed in figure 4(b) in the region near and below $X = 1$ for values of Y only slightly greater than 1. These peculiarities in the $\mu'(h)$ profiles give rise to the interesting Z traces seen in figures 9, 10, and 11. To produce the detailed variations seen in these figures, lamination thicknesses of 20 km had to be used to provide adequate frequency resolution. However, only the 100 km (fig. 9(a)) and 40 km (fig. 10(a)) "cumulative delay" curves are shown. The Z trace with a smooth, monotonic variation of virtual depth with frequency, shown in figure 9(b), is most frequently observed in topside ionograms. On the other hand, figure 10(b) shows the development of a "plateau" in the Z trace. At low frequencies the variation is smooth, as in figure 9(b), with the largest delay in the lamination of wave reflection. At f near 0.29 Mc/s, where the $\mu'(h)$ maximum first occurs (shown as a dotted line), a precipitous increase in virtual depth is observed. For $0.29 \text{ Mc/s} < f < f_{Z\infty}$, the virtual depth remains relatively constant. In this region the largest relative delay is provided by that lamination exhibiting the $\mu'(h)$ maximum. As f approaches $f_{Z\infty}$, the normal rapid increase in virtual depth is again observed with the largest delay occurring in the lamination immediately below the satellite. These features, although not quite as drastic, are seen in the Z trace in figure 11 simulated for an Alouette I ionogram.

These peculiar Z traces occur at rather low frequencies where the Alouette sounder response is weak and at high latitudes where ionograms are normally poor. Also, the delays become quite large and some of them would only be observable on a "second-time-around" basis. Thus actual observation of these shapes is relatively infrequent. With improved sounder design for future satellites, however, observation should be possible and its use for $N(h)$ reduction become feasible.

The entire set of computed ionograms (ordinary, extraordinary, and Z traces) for all eight cases are shown in figures 12 through 19. The low-altitude ionograms are plotted on a linear frequency scale simulating Alouette I ionograms. The high-altitude ionograms are plotted on two different linear frequency scales for below and above 2 Mc/s, simulating Alouette II ionograms.

DISCUSSION

Figures 12 through 19 illustrate most types of ionogram traces due to vertical propagation which are observed in Alouette I and Alouette II sounder data. At $h' = 0$ the traces always occur such that $f_{XS} > f_{OS} > f_{ZS}$ and $(dh'_X/df) = (dh'_O/df) = dh'_Z/df = \infty$. Although the cusps are often observed on ionograms from both Alouette I and Alouette II, they appear only in the simulated high-altitude ionograms shown in this study. It can be shown that the plasma scale height, defined by $-N(dN/dh)^{-1}$, must have a height gradient near the satellite that exceeds a certain critical value for the cusp to appear

(J. Shmoys, private communication). Because the model profiles are not defined below 400 km, F₂ layer penetration is not simulated on the computed ionograms. The ionograms shown were computed for profiles having lamination thicknesses of 100 km and 40 km for Alouette II and Alouette I, respectively, corresponding to a total of 27 and 16 "scaled" points (or 26 and 15 laminations).

It is difficult, in practice, to prescribe ionogram scaling criteria for optimum N(h) computation. It is, in principle, desirable to scale the ionogram trace so that the computed N(h) profile has laminations of equal thickness, say, of about 100 km for Alouette II and of about 50 km for Alouette I data. This would require a total of about 25 points for the former and 15 points for the latter ionograms. Computation times on large computers are then typically a few seconds, which is reasonable for the vast number of topside ionograms available for study. The "equal lamination thickness" scaling criterion is impossible to apply strictly since, a priori, the N(h) profile is unknown. However, the models studied do illustrate that, for this criterion, the scaling procedures are quite different for the cusp and no-cusp cases. For no-cusp, the scaled points are separated by approximately equal intervals along the traces. For the cusp, the scaled points are thinned out in spacing where the trace curvature is small and packed in spacing where the curvature is large - the greater the curvature, the closer the packing.

Although the simulated high-altitude Alouette II ionograms (figs. 12-15) and Alouette I ionograms (figs. 16-19) have many similarities, they have subtle differences that are observable in both simulated and actual ionograms. The Alouette II sounder frequency sweep rate below 2 Mc/s is about six times slower than the Alouette I sweep rate. Thus, greater frequency resolution is available in the regions where the large slopes occur. Although in principle the virtual depth resolution is identical for the two sounders because of identical pulse widths, in practice the resolution is poorer on Alouette II ionograms since the virtual depth range coordinate, of about 4500 km, occupies the same film dimension as does the 1500 km virtual depth range for Alouette I. Therefore, the available $h'(f)$ resolutions are about the same for Alouette I and II ionograms. However, the plasma scale height increases with altitude in the topside ionosphere, and the Alouette II trace may have much larger virtual depths and slopes immediately above f_{xs} , f_{os} , and f_{zs} . The available resolutions which are enough to yield accurate computed N(h) profiles for most of the Alouette I ionograms are not sufficient for many high-altitude Alouette II ionograms. Much more accurate and careful analysis is required.

Extraordinary traces in topside ionograms are usually continuous and complete while the ordinary trace generally exhibits gaps between the plasma frequency (or the gyrofrequency when $f_{hs} > f_n$) and upper-hybrid frequency, due to antenna impedance mismatch, and the Z trace is usually weak, due to noise, interference and low sounder sensitivity, and/or excessive dispersion. Thus, the extraordinary trace is generally used, and for Alouette I is the only trace which has been used, for routine N(h) reduction. In actual ionograms a single reflection trace for each propagation mode is normally observed and, in most cases, the traces are due to vertical propagation. However, traces due to oblique propagation may appear with or without the appearance of

a vertical propagation trace. For high-altitude Alouette II ionograms, because of the scaling accuracy difficulties and because of the frequent appearance of multiple traces, particularly for the extraordinary mode, it would be desirable to include the ordinary and Z trace data in the reduction procedures. Comparison of figures 12 through 19 shows that the general shape of the extraordinary trace remains quite stable from case to case, certainly more so than the ordinary and Z traces. As mentioned earlier, the extraordinary group refractive index is a more sensitive function to Y than θ , while the ordinary group refractive index is more sensitive to θ than Y . The variation of Y (i.e., f_h) is quite small during the passage of the satellite over one telemetry recording station whereas θ may change significantly. The sensitivity of the ordinary trace to θ is further illustrated in figure 20. Here the computed ordinary traces for case 1 are shown for the same f_n and f_h model profiles but with θ allowed to vary from 5° to 30° . Hence, this difference in sensitivity of each mode to the magnitude and angle of the magnetic field vector indicates that the use of redundant data may improve the accuracy of computed $N(h)$ profiles.

An operationally feasible closed-loop reduction procedure that uses redundant data to improve computed $N(h)$ profile accuracy and/or operator confidence is summarized as follows: (1) Scale the extraordinary trace; (2) compute an $N(h)$ profile therefrom; (3) compute ordinary and Z traces from the computed $N(h)$ profile; (4) compare the computed ordinary and Z traces with the visible portions of those traces on the ionogram; (5) if necessary, correct the extraordinary trace scaled points and repeat this procedure until the comparisons in step (4) agree. Since the satellite moves in position while the traces are being formed this comparison becomes questionable should the $N(h)$ distribution drastically change during this period.

Another useful procedure is to (1) scale the extraordinary and Z traces with a least-squares fitting technique to deduce an accurate $N(h)$ profile near the satellite; (2) from this partial profile compute the ordinary trace to bridge the gap where that trace is not observed; (3) continue the $N(h)$ reduction using the ordinary trace, in conjunction with the extraordinary trace if necessary. The particular advantages of this approach are that (a) the ordinary trace is normally spread and dispersed much less than the extraordinary trace and (b) the ordinary trace more likely results from vertical propagation.

Yet another approach would be to (1) scale the visible portion of the three traces; (2) compute a profile from each; and (3) combine the three individual profiles in a least-squares manner to compute a final $N(h)$ profile.

For those high-altitude ionograms in which the visible traces are all due to oblique propagation, the above procedures will not yield accurate profiles. Then, ray tracing analyses must be performed to determine the ionospheric distribution.

A data reduction system, called FILMCLIP, is currently operational at Ames Research Center and incorporates the features mentioned.

Ames Research Center

National Aeronautics and Space Administration

Moffett Field, Calif. 94035, May 6, 1968

188-39-01-01-00-21

APPENDIX A

REFRACTIVE INDEX EQUATIONS

The group refractive index defined by

$$\mu' \equiv c/v_g \quad (A1)$$

is obtained from the phase refractive index

$$\mu \equiv c/v_p \quad (A2)$$

by the process

$$\mu' = d(\mu f)/df \quad (A3)$$

where

c velocity of light in free space

v_g group velocity of the electromagnetic wave

v_p phase velocity of the electromagnetic wave

f sounder frequency

The collisionless phase refractive index is given by the Appleton-Hartree equation of the magnetoionic theory (ref. 3):

$$\mu = \left[1 - \frac{X}{1 - \frac{Y^2 \sin^2 \theta}{2(1 - X)} \pm \sqrt{\frac{Y^4 \sin^4 \theta}{4(1 - X)^2} + Y^2 \cos^2 \theta}} \right]^{1/2} \quad (A4)$$

where

X $f_n^2/f^2 = N/12,400f^2$

N electron concentration, electrons/cm³

f_n electron plasma frequency, Mc/s

Y $f_h/f = 2.8 B/f$

B magnetic induction of earth's field, gauss

f_h electron gyrofrequency, Mc/s

θ angle between the wave normal and earth's magnetic field directions
 ($\theta = 90^\circ - I$, where I is the magnetic dip, for vertical propagation
 in a stratified ionosphere)

It can be seen that two modes of propagation are possible in a magnetoionic medium, the ordinary mode (with the plus sign) and the extraordinary mode (with the minus sign). These are usually denoted with appropriate subscripts x and o . For clarity, the ordinary and extraordinary phase refractive indices may be written:

$$\mu_o = \left(1 - \frac{X}{S_o}\right)^{1/2} \quad (A5)$$

$$\mu_x = \left(1 - \frac{X}{S_x}\right)^{1/2} \quad (A6)$$

where

$$S_o = 1 - \frac{Y^2 \sin^2 \theta}{2(1 - X)} + \frac{YR}{2(1 - X)} \quad (A7)$$

$$S_x = 1 - \frac{Y^2 \sin^2 \theta}{2(1 - X)} - \frac{YR}{2(1 - X)} \quad (A8)$$

$$R = [Y^2 \sin^4 \theta + 4 \cos^2 \theta (1 - X)^2]^{1/2} \quad (A9)$$

Applying equation (A3) to equations (A5) through (A9) yields the ordinary and extraordinary group refractive indices:

$$\mu_o' = \frac{1}{\mu_o} \left\{ 1 - \frac{XY(1 - X)\cos^2 \theta}{S_o^2(Y \sin^2 \theta + R)} \left[1 - \frac{Y \sin^2 \theta}{R} \left(\frac{1 + X}{1 - X} \right) \right] \right\} \quad (A10)$$

$$\mu_x' = \frac{1}{\mu_x} \left\{ 1 + \frac{X(1 - S_x)}{2S_x^2} \left[1 + \frac{Y \sin^2 \theta}{R} \left(\frac{1 + X}{1 - X} \right) \right] \right\} \quad (A11)$$

These equations simplify considerably for the special cases of transverse propagation ($\theta = 90^\circ$) and longitudinal propagation ($\theta = 0^\circ$):

(a) Transverse propagation

$$\mu_o = (1 - X)^{1/2} \quad (A12)$$

$$\mu_x = \left[1 - \frac{X(1 - X)}{1 - X - Y^2} \right]^{1/2} \quad (A13)$$

$$\mu_o' = \frac{1}{\mu_o} \quad (A14)$$

$$\mu_x' = \frac{1}{\mu_x} \left[1 + \frac{XY^2}{(1 - X - Y^2)^2} \right] \quad (A15)$$

(b) Longitudinal propagation

$$\mu_o = \left(1 - \frac{X}{1 + Y} \right)^{1/2} \quad (A16)$$

$$\mu_x = \left(1 - \frac{X}{1 - Y} \right)^{1/2} \quad (A17)$$

$$\mu_o' = \frac{1}{\mu_o} \left[1 - \frac{XY}{2(1 + Y)^2} \right] \quad (A18)$$

$$\mu_x' = \frac{1}{\mu_x} \left[1 + \frac{XY}{2(1 - Y)^2} \right] \quad (A19)$$

Both μ_x and μ_x' for the longitudinal case exhibit discontinuities at $X = 1$ when $Y > 1$, that is, where the extraordinary mode is generally known as the Z mode. It can be shown (ref. 4) that the following relationships result:

$$\mu_x = \mu_z = \left(1 - \frac{X}{1 - Y} \right)^{1/2} \quad \text{for} \quad X < 1 \quad (A20)$$

$$= \left(1 - \frac{X}{1 + Y} \right)^{1/2} \quad \text{for} \quad X > 1 \quad (A21)$$

$$\mu'_x = \mu'_z = \frac{1}{\mu_z} \left[1 + \frac{XY}{2(1 - Y)^2} \right] \quad \text{for} \quad X < 1 \quad (\text{A22})$$

$$= \frac{1}{\mu_z} \left[1 - \frac{XY}{2(1 + Y)^2} \right] \quad \text{for} \quad X > 1 \quad (\text{A23})$$

For $\theta \neq 0^\circ$ and $Y > 1$, μ'_z exhibits a maximum at $X = 1$ and can be approximated by

$$\mu'_z \cong 1 + \frac{1}{Y^2 \sin^2 \theta} \quad (\text{A24})$$

APPENDIX B

COMPUTATIONAL PROCEDURES

Appendix A summarizes the equations for μ' as functions of X , Y , and θ . For any frequency, f , profiles of X and Y are simply computed from the given $f_n(h)$ and $f_h(h)$ models, and θ is assumed height invariant. The heights of reflection, h_r , for the ordinary, extraordinary, and Z modes are given as the heights where $X = 1$, $1 - Y$, and $1 + Y$, respectively. Hence, all quantities on the right-hand side of equation (1) are known and the integration for virtual depth, at that frequency, is easily calculated. In actual ionogram analysis where h_r is the unknown, given h' , the situation is more complex. Since the parameter Y appears in the integrand and its integral upper limit, an iteration scheme is required to insure convergence to the correct reflection height (ref. 1).

The cumulative delay curves and ionogram traces were calculated for the $f_n(h)$ and $f_h(h)$ models by numerically integrating equation (1) on a digital computer. The f_n profiles were divided into 100 km and 40 km laminations for the high-altitude (3000 km) and low-altitude (1000 km) profiles. Equation (1) was then solved for those frequencies for each propagation mode having reflection heights that occur at the lower boundary of each lamination. Within each lamination the parabolic-in-log X assumption was used, that is, in the $(i + 1)$ st lamination:

$$h = h_i + a_{i+1} \log \frac{X}{X_i} + b_{i+1} \left(\log \frac{X}{X_i} \right)^2 \quad (B1)$$

where h_i and X_i are the values at the upper boundary of that lamination. The gyrofrequency was assumed to have an inverse-cube variation between its values at the upper and lower boundaries. Continuity in slope was assured at each boundary by the condition:

$$a_{i+1} = a_i + 2b_i \log \frac{X_i}{X_{i-1}} \quad (B2)$$

A parabolic-in-log X starting procedure was also used. Since no boundary condition is available at the sounder, however, the first two laminations are used to define the initial parabolic variation.

Applying these lamination techniques, equation (1) becomes

$$h'_c(f) = \sum_{i=1}^M \int_{h_i}^{h_{i+1}} \mu' dh ; M = 2, 3, 4, \dots, N - 1 \quad (B3)$$

and

$$h'(f) = \sum_{i=1}^{N-1} \int_{h_i}^{h_{i+1}} \mu' dh \quad (B4)$$

where h'_c is "cumulative delay," $N - 1$ is the lamination number, and $h_1 = h_s$.

Since μ' becomes infinite at the reflection heights (and at the sounder for $f_{z\infty}$), special care must be taken for accurate integration. Changes of variables are made in those lamina where μ' becomes infinite such that the modified integrand is finite. These variable changes are given by:

$$t_O^2 = 1 - X \quad \text{for all laminations in the ordinary mode}$$

$$t_X^2 = 1 - \frac{X}{1 - Y_r} \quad \text{for all laminations in the extraordinary mode}$$

$$t_Z^2 = 1 - \frac{1 - Y^2}{(1 - Y^2 \cos^2 \theta)X} \quad \text{for the first lamination in the Z mode, and}$$

$$t_Z^2 = 1 - \frac{X}{1 + Y_r} \quad \text{for all but the first lamination in the Z mode}$$

where Y_r is the value of Y at the height of reflection. Gaussian quadrature is used to evaluate the modified equation (B3) and (B4) integrals. It has been shown that, in general, three-point gaussian coefficients provide sufficient accuracy (ref. 1). However, for small θ higher order gaussian quadratures are required for the ordinary mode. In general, it suffices to use

3-point gaussian for $\theta \geq 40^\circ$

7-point gaussian for $10^\circ \leq \theta < 40^\circ$

16-point gaussian for $\theta < 10^\circ$

REFERENCES

1. Jackson, J. E.: Reduction of Topside Ionograms to Electron Density Profiles. Proc. IEEE, June 1969.
2. Paul, A. K.: Ionospheric Electron-Density Profiles With Continuous Gradients and Underlying Ionization Corrections. I. The Mathematical-Physical Problem of Real-Height Determination From Ionograms. *Radio Sci.*, vol. 2, Oct. 1967, pp. 1135-1158.
3. Ratcliffe, J. A.: The Magneto-Ionic Theory and Its Applications to the Ionosphere. Cambridge Univ. Press, 1959.
4. Whale, H. A.; and Stanley, J. P.: Group and Phase Velocities From the Magneto-Ionic Theory. *J. Atmospheric Terrest. Phys.*, vol. 1, 1950, pp. 32-94.
5. Shinn, D. H.; and Whale, H. A.: Group Velocities and Group Heights From the Magneto-Ionic Theory. *J. Atmospheric Terrest. Phys.*, vol. 2, 1952, pp. 85-105.
6. Becker, W.: Tables of Ordinary and Extraordinary Refractive Indices, Group Refractive Indices and $h'_{O,X}(f)$ Curves for Standard Ionospheric Layer Models. Max-Planck-Institute für Aeronomie, Berlin, Springer, no. 4, 1960.
7. Colin, Lawrence; Chan, Kwok-Long; and Lee, Jack G. K.: Phase and Group Refractive Indices From the Collisionless Magnetoionic Theory. NASA TM X-1553, 1967.

TABLE I.- PLASMA AND GYROFREQUENCY MODELS

Case	h_s , km	Description	θ , deg	f_{ns} , Mc/s	N_s , cm^{-3}	f_{hs} , Mc/s	Simulation of
1	3000	high f_n , high f_h	5	0.64	5×10^3	0.50	Alouette II apogee, high latitude, day
2	3000	low f_n , low f_h	55	0.28	10^3	0.30	Alouette II apogee, low latitude, night
3	3000	high f_n , low f_h	55	0.64	5×10^3	0.30	Alouette II apogee, low latitude, day
4	3000	low f_n , high f_h	5	0.28	10^3	0.50	Alouette II apogee, high latitude, night
5	1000	high f_n , high f_h	5	1.49	2.8×10^4	1.03	Alouette I, high latitude, day
6	1000	low f_n , low f_h	55	0.66	5.6×10^3	0.62	Alouette I, low latitude, night
7	1000	high f_n , low f_h	55	1.49	2.8×10^4	0.62	Alouette I, low latitude, day
8	1000	low f_n , high f_h	5	0.66	5.6×10^3	1.03	Alouette I, high latitude, night

Note: The subscript s denotes values of the quantities appropriate to the location of a hypothetical sounder.

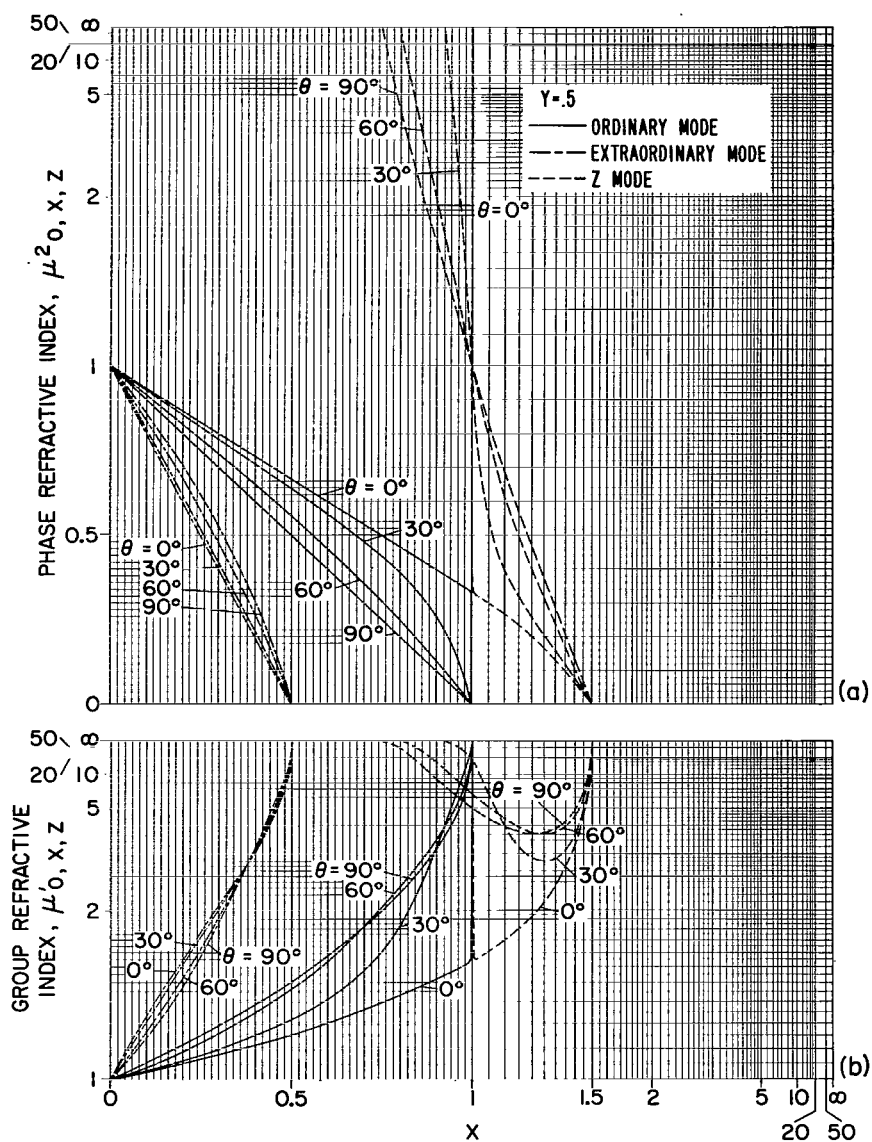


Figure 1.- Graphs of (a) μ^2 and (b) μ' versus X for $Y = 0.5$ for $\theta = 0^\circ, 30^\circ, 60^\circ, 90^\circ$.

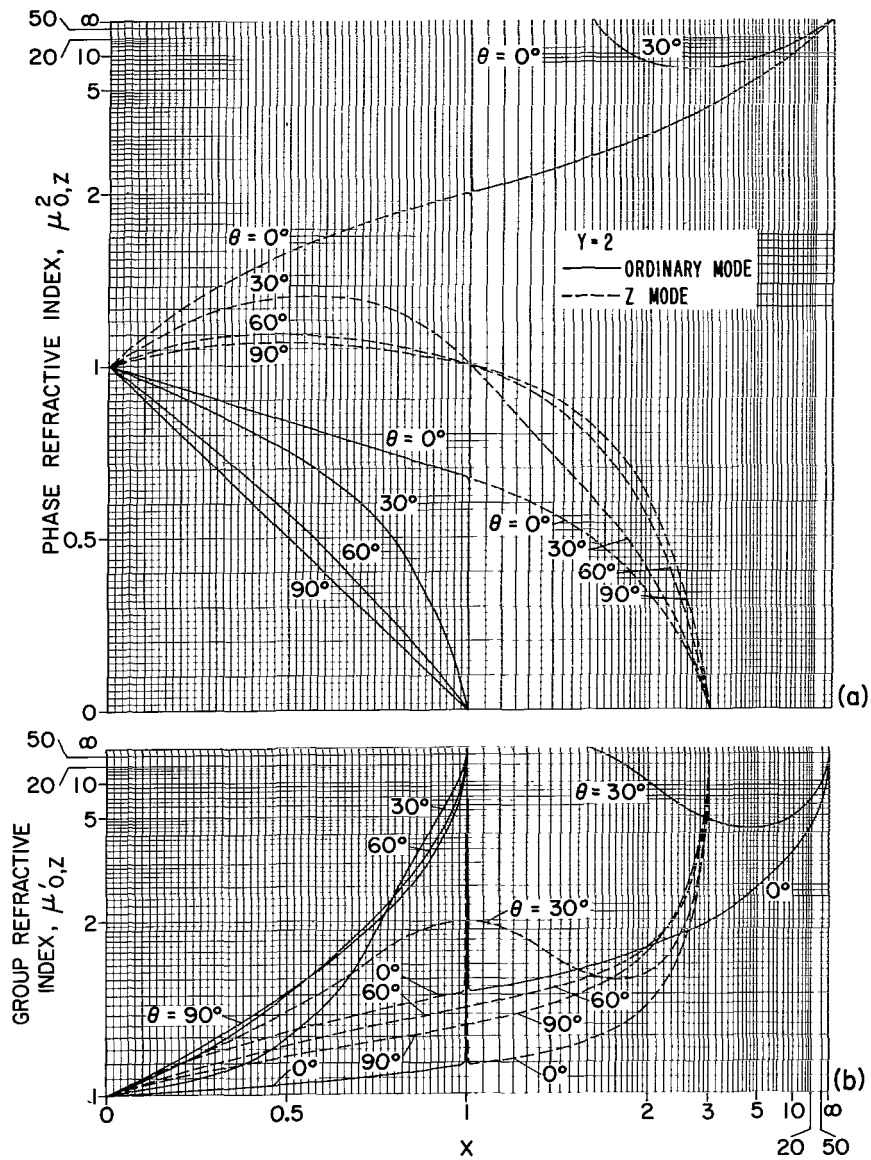


Figure 2.- Graphs of (a) μ^2 and (b) μ' versus X for $Y = 2$ for $\theta = 0^\circ, 30^\circ, 60^\circ, 90^\circ$.

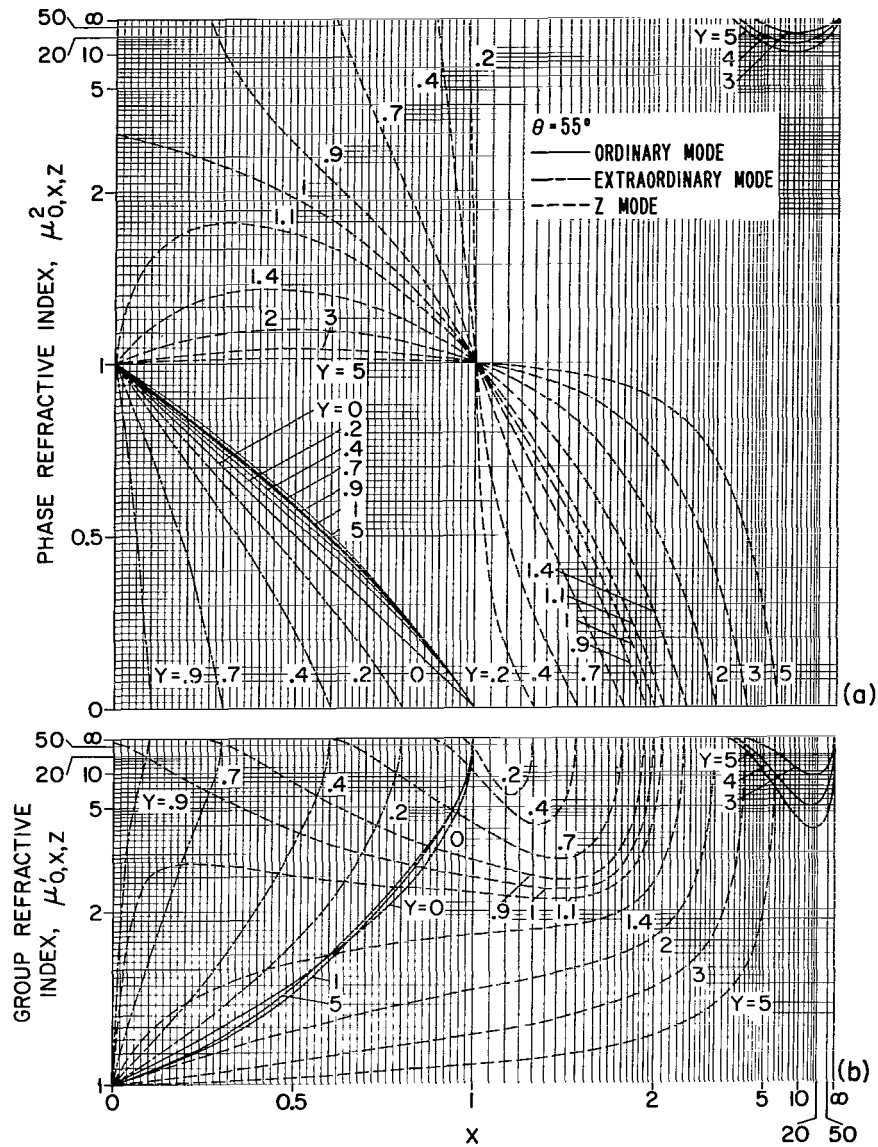


Figure 4.- Graphs of (a) μ^2 and (b) μ' versus X for $\theta = 55^\circ$ and values of Y .

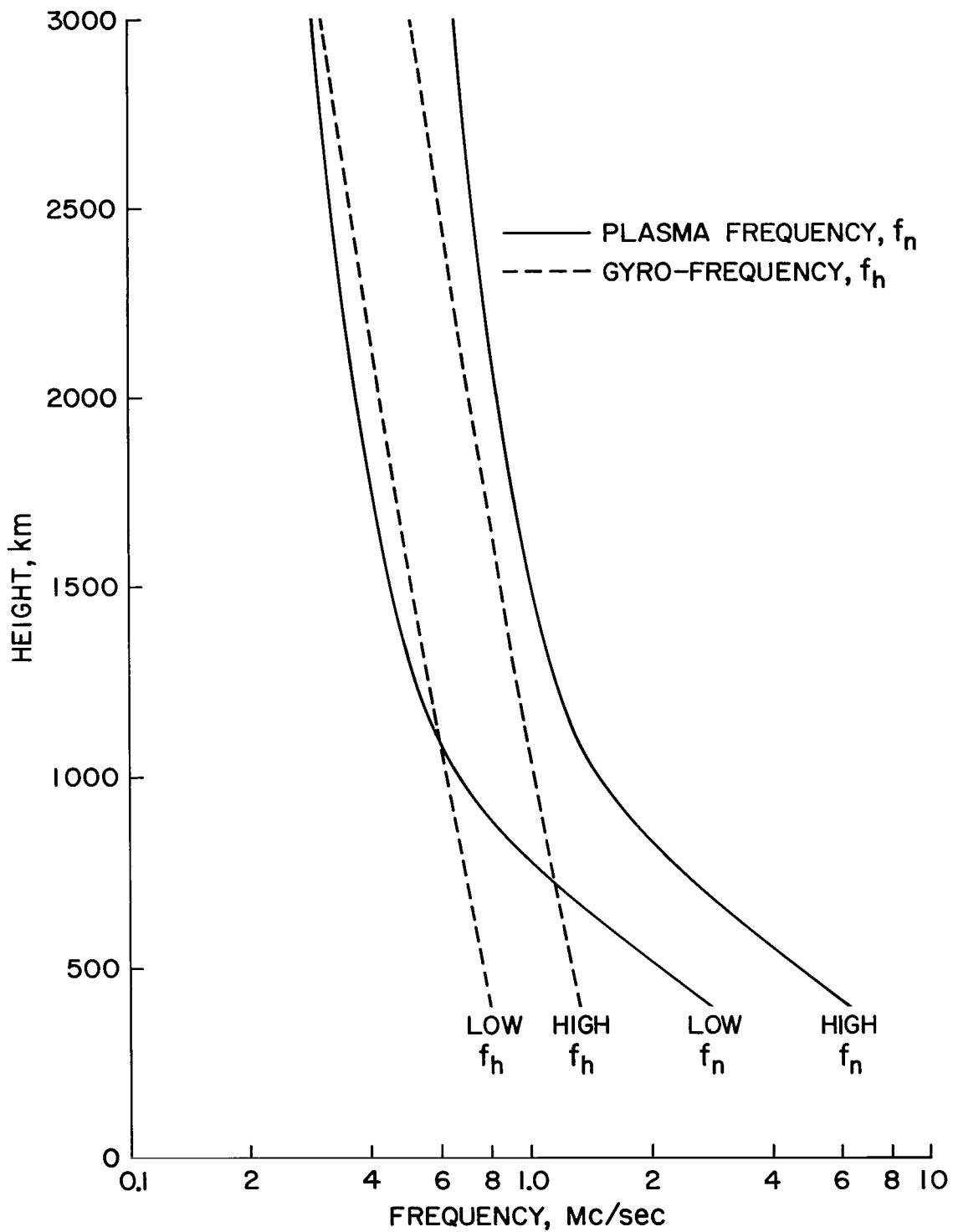


Figure 5.- Model profiles of plasma frequency, f_n , and gyrofrequency, f_h .

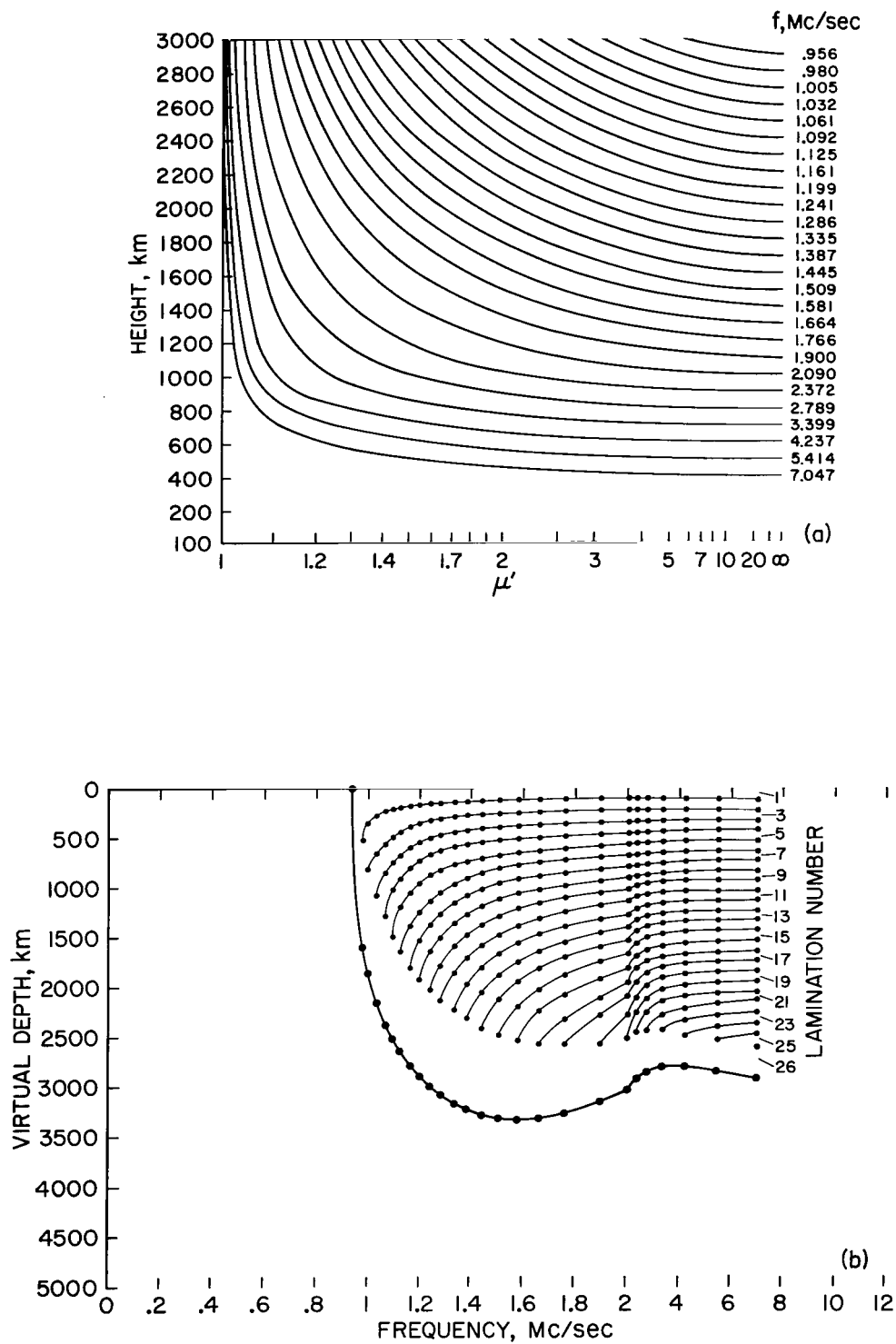


Figure 6.- (a) μ'_x versus h and (b) $h'_x = \int \mu'_x dh$ versus f for case 1. Cumulative delay curves for 100-km laminations are also shown in part (b).

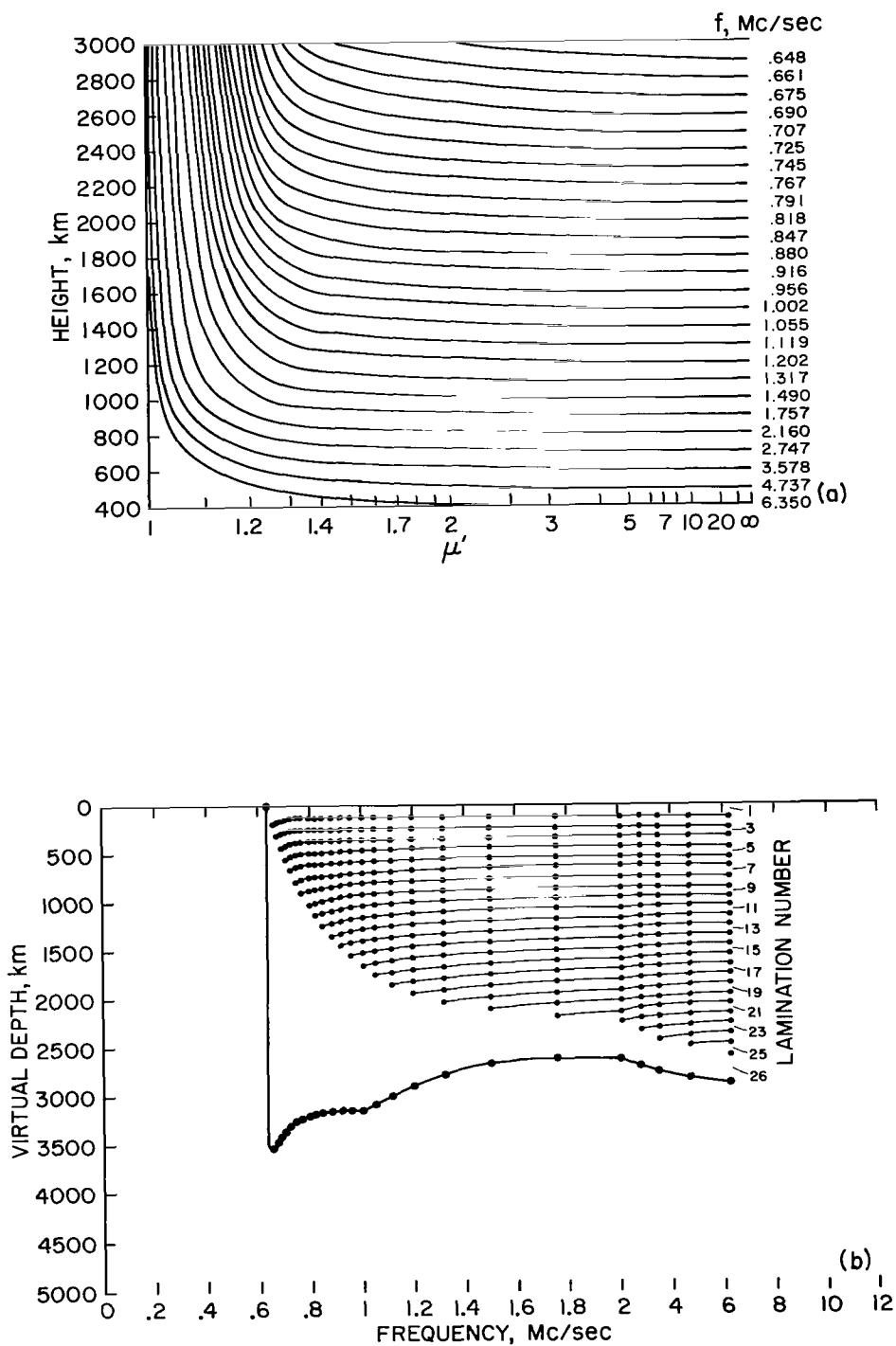


Figure 7.- (a) μ'_0 versus h and (b) $h'_0 = \int \mu'_0 dh$ versus f for case 1. Cumulative delay curves for 100-km laminations are also shown in part (b).

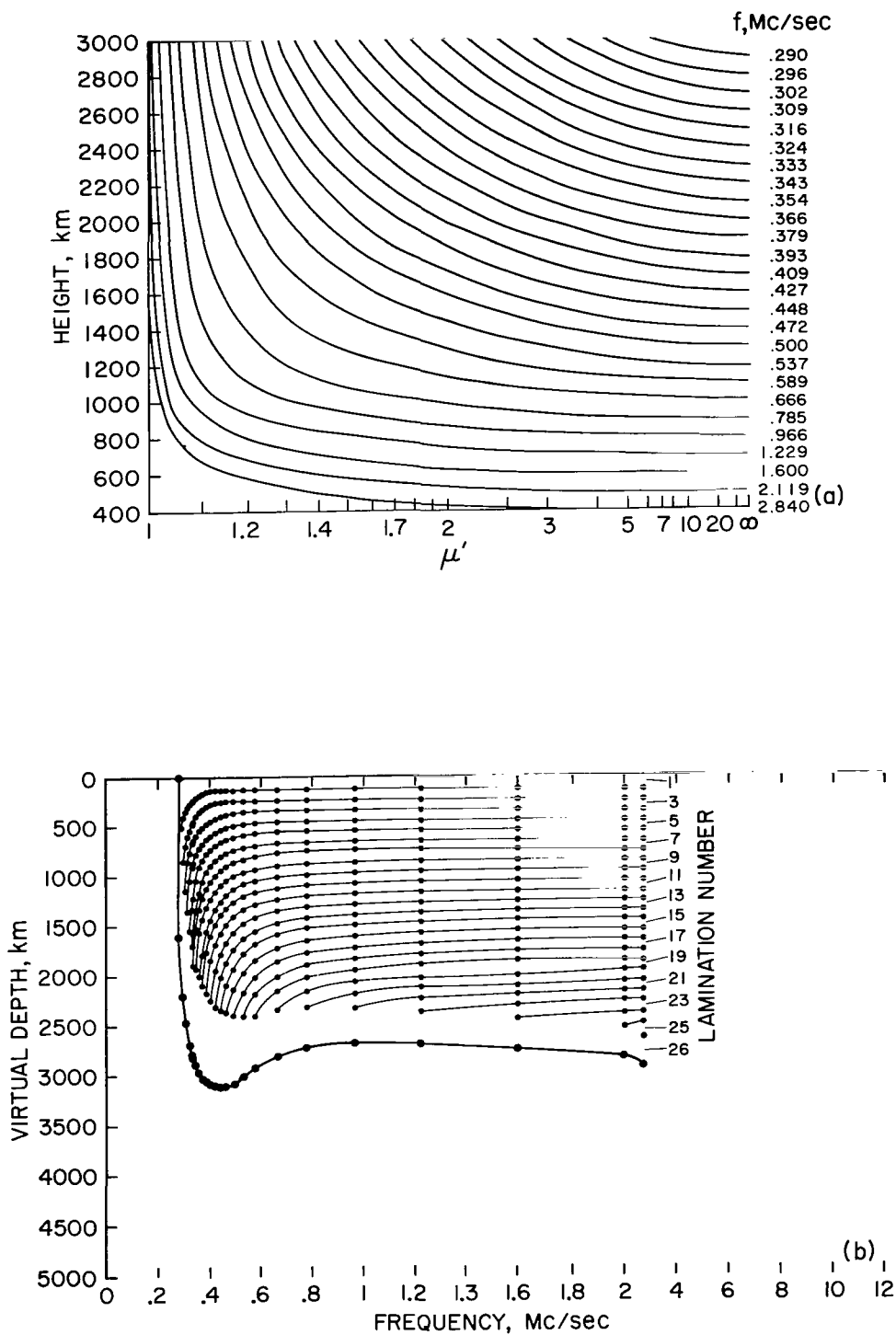


Figure 8.- (a) μ'_0 versus h and (b) $h'_0 = \int \mu'_0 dh$ versus f for case 2. Cumulative delay curves for 100-km laminations are also shown in part (b).

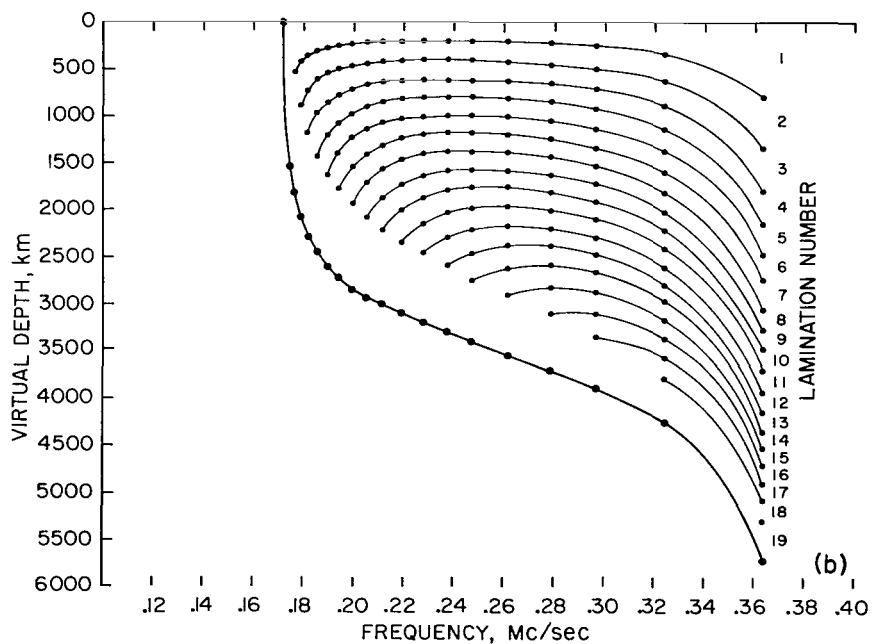
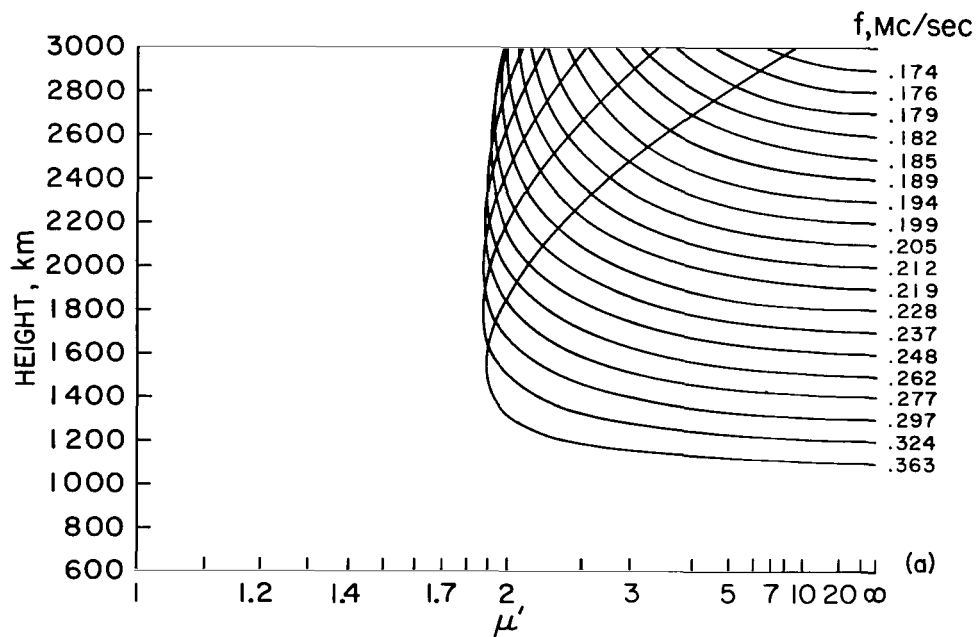


Figure 9.- (a) μ'_z versus h and (b) $h'_z = \int \mu'_z dh$ versus f for case 2. Cumulative delay curves for 100-km laminations are also shown in part (b).

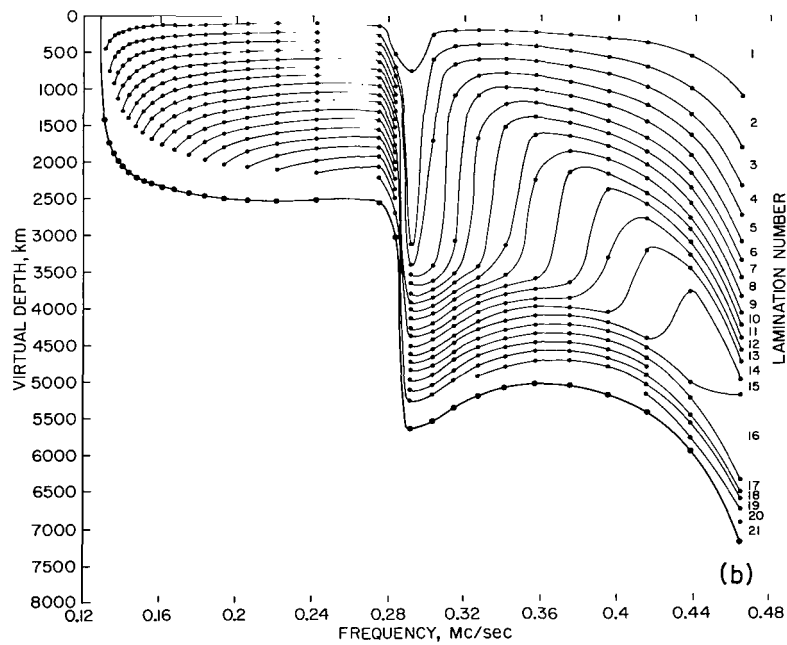
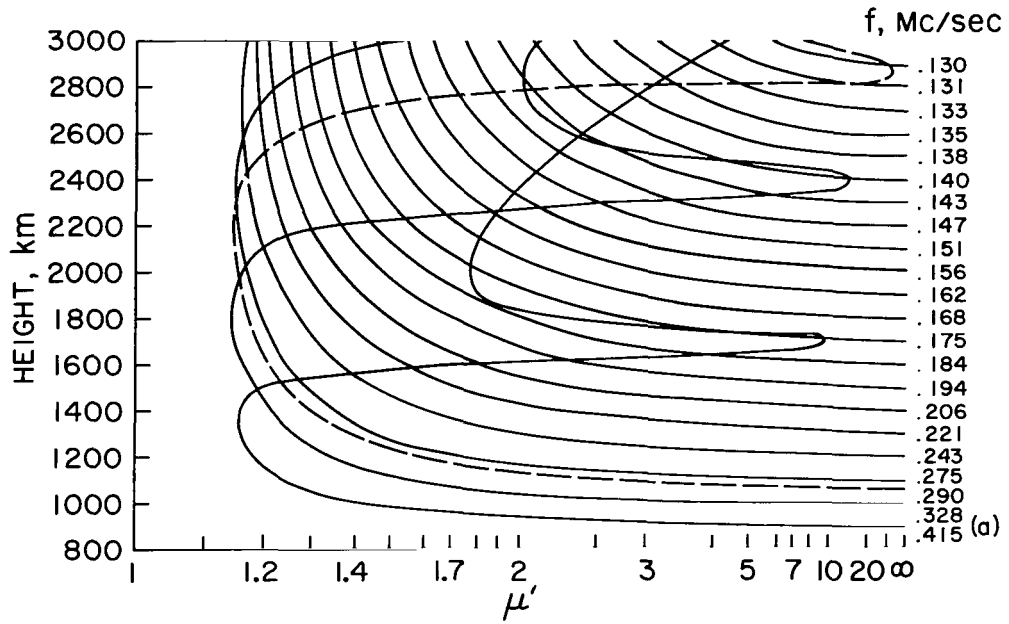


Figure 10.- (a) μ'_z versus h and (b) $h'_z = \int \mu'_z dh$ versus f for case 4. Cumulative delay curves for 100-km laminations are also shown in part (b).

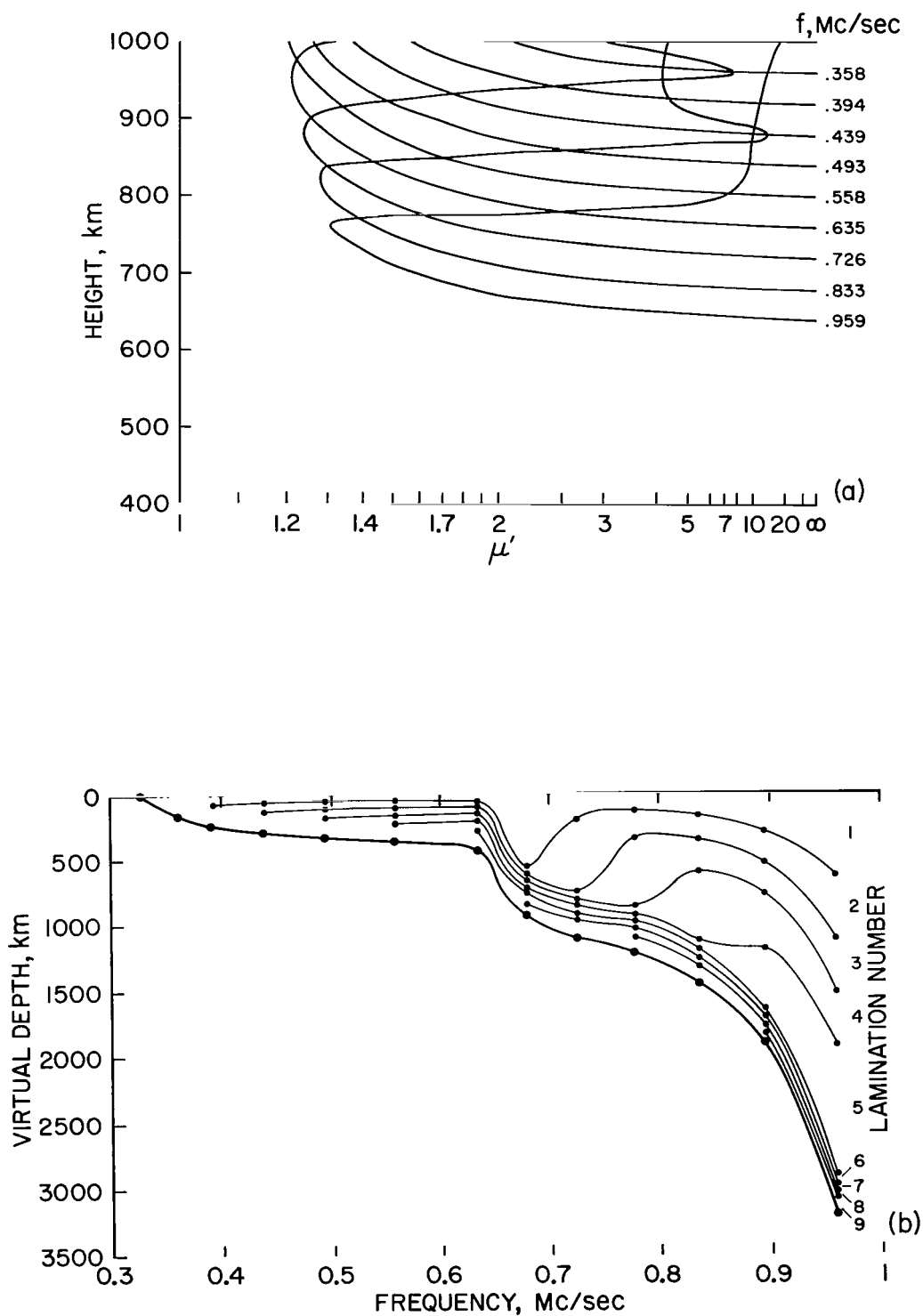


Figure 11.- (a) μ'_z versus h and (b) $h'_z = \int \mu'_z dh$ versus f for case 8. Cumulative delay curves for 40-km laminations are also shown in part (b).

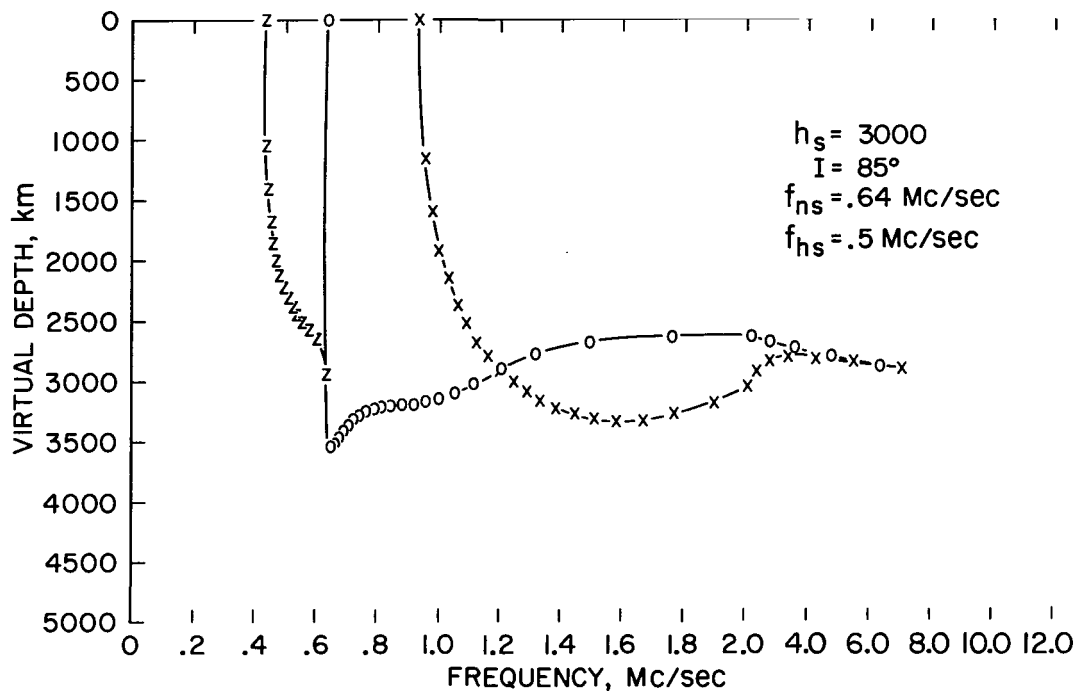


Figure 12.- Computed ordinary, extraordinary, and Z traces for case 1.

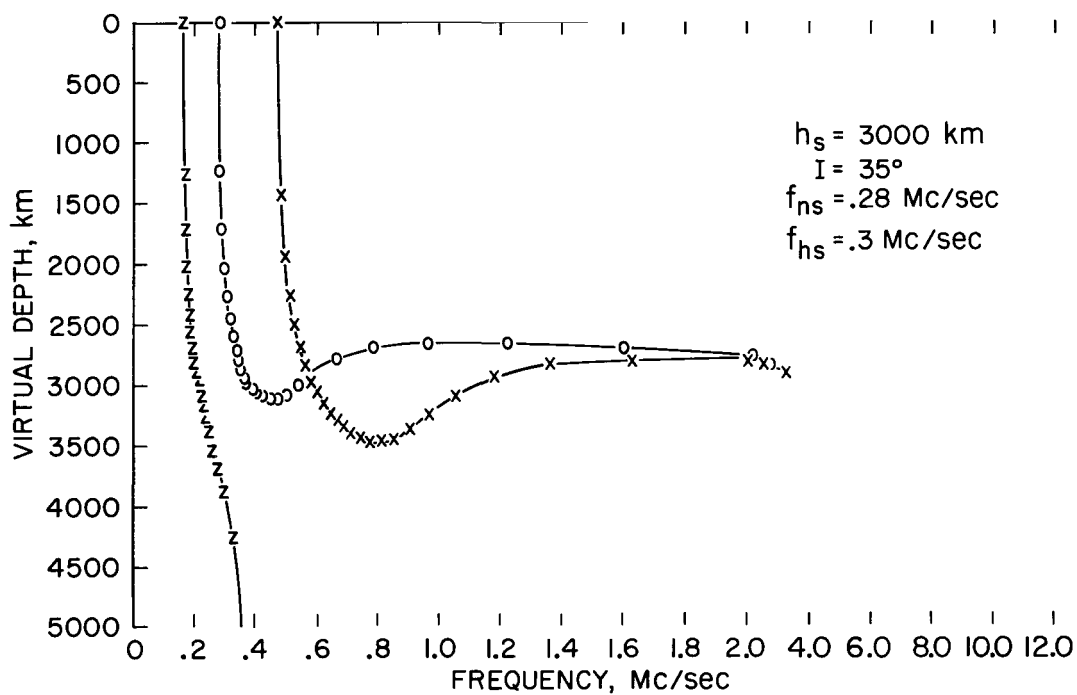


Figure 13.- Computed ordinary, extraordinary, and Z traces for case 2.

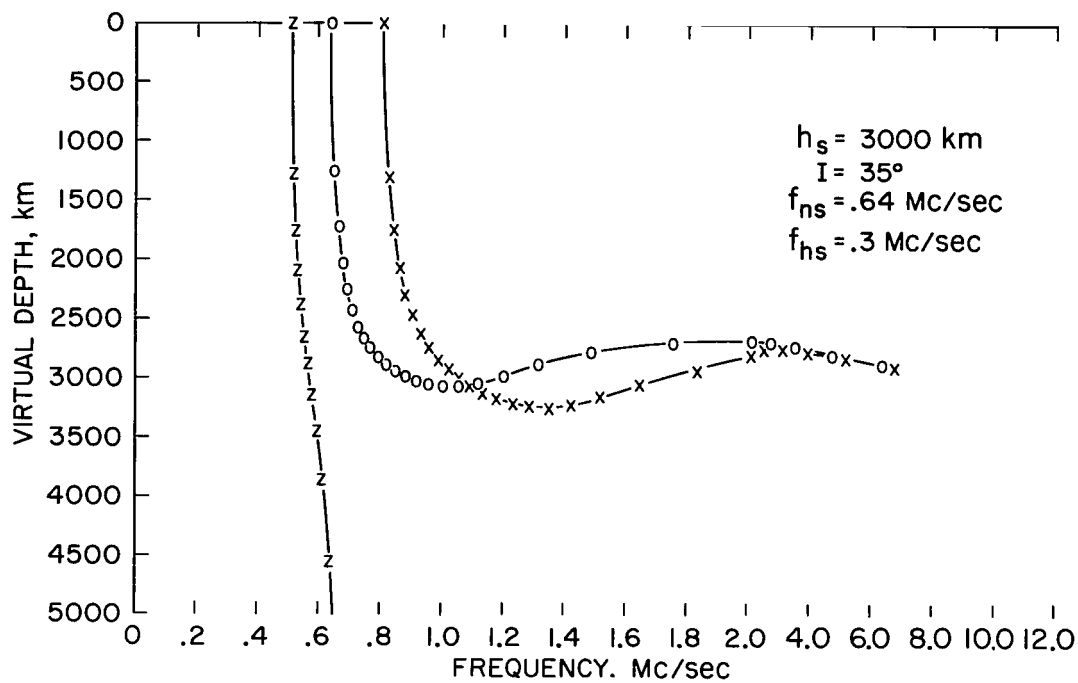


Figure 14.- Computed ordinary, extraordinary, and Z traces for case 3.

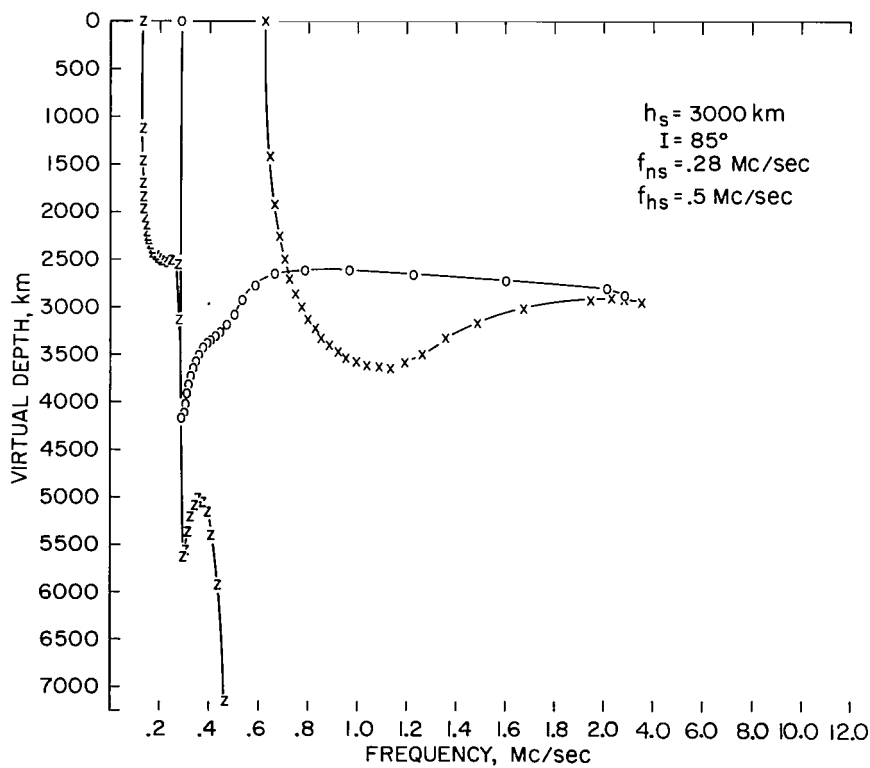


Figure 15.- Computed ordinary, extraordinary, and Z traces for case 4.

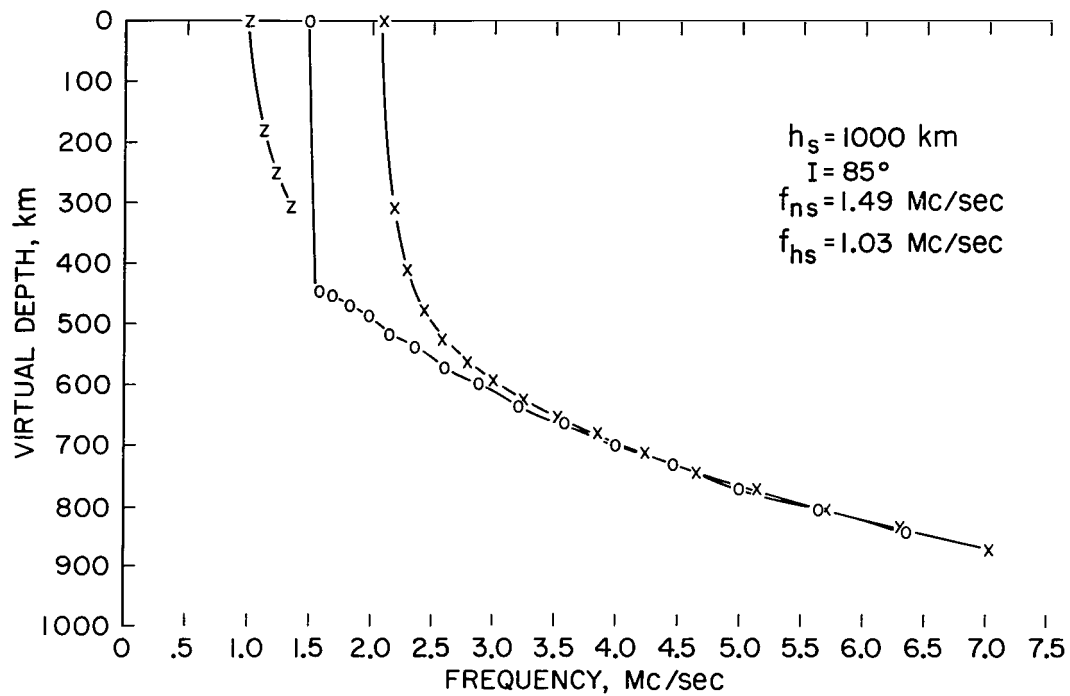


Figure 16.- Computed ordinary, extraordinary, and Z traces for case 5.

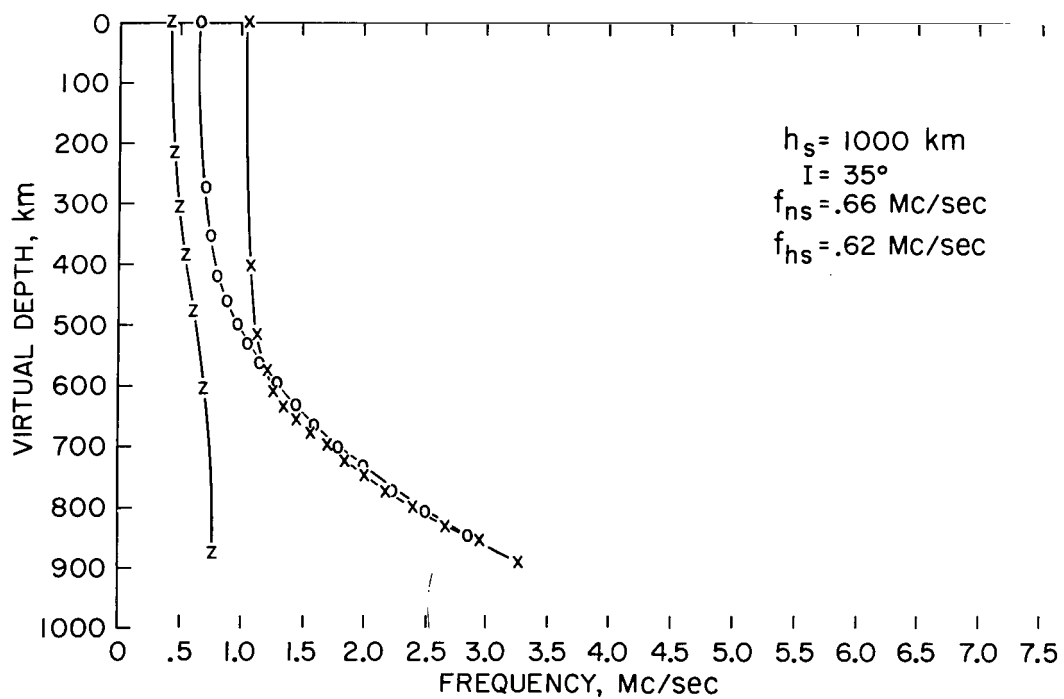


Figure 17.- Computed ordinary, extraordinary, and Z traces for case 6.

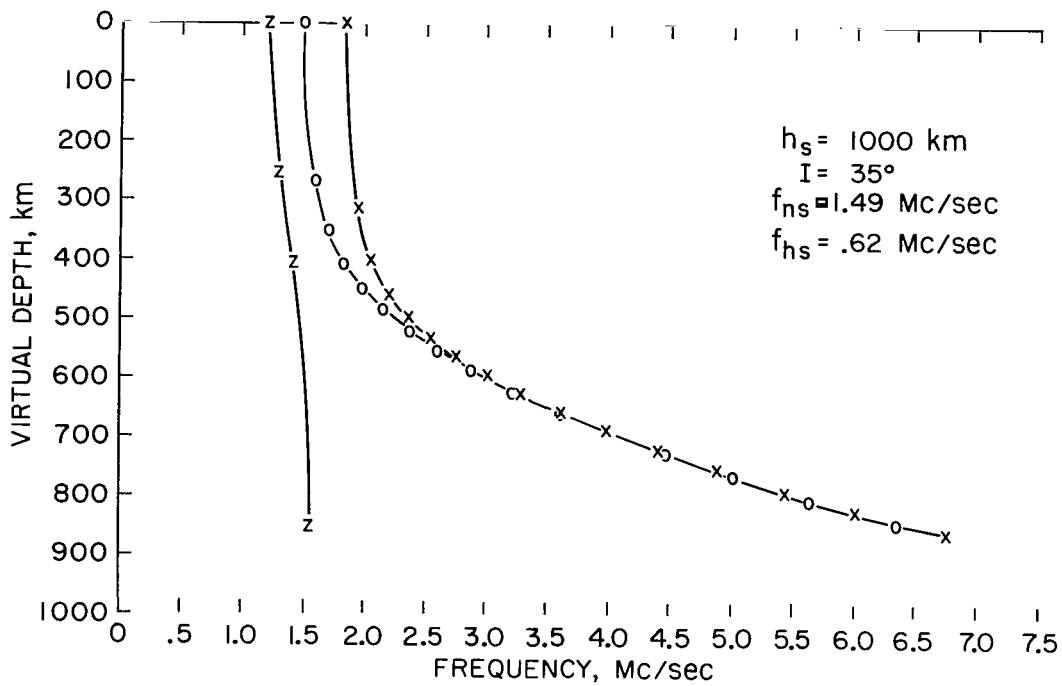


Figure 18.- Computed ordinary, extraordinary, and Z traces for case 7.

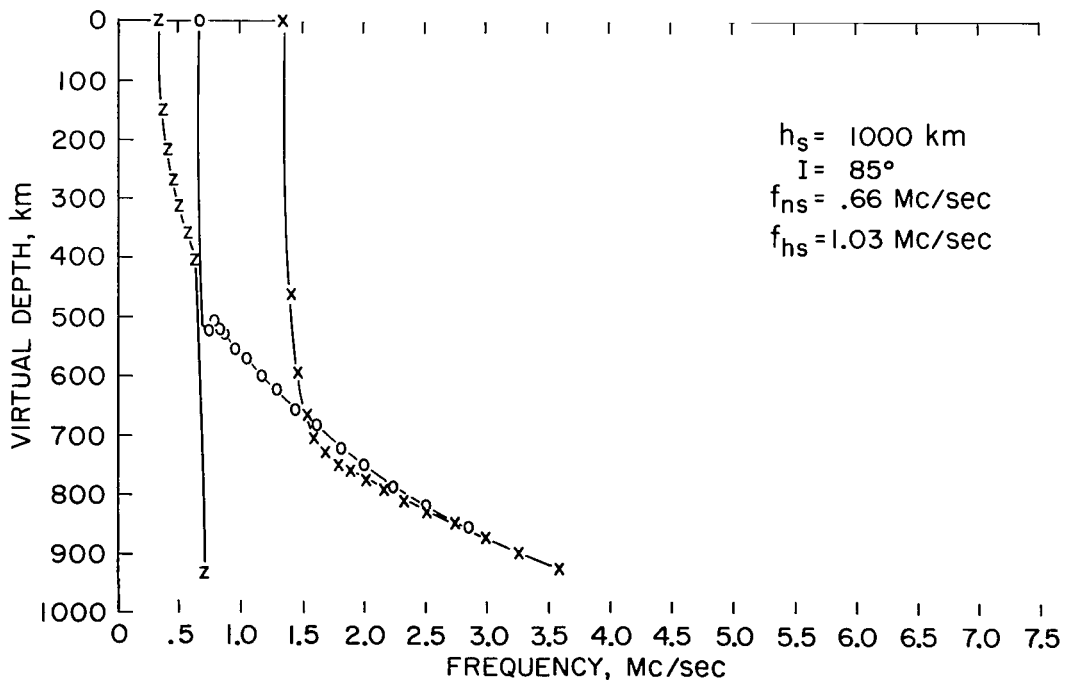


Figure 19.- Computed ordinary, extraordinary, and Z traces for case 8.

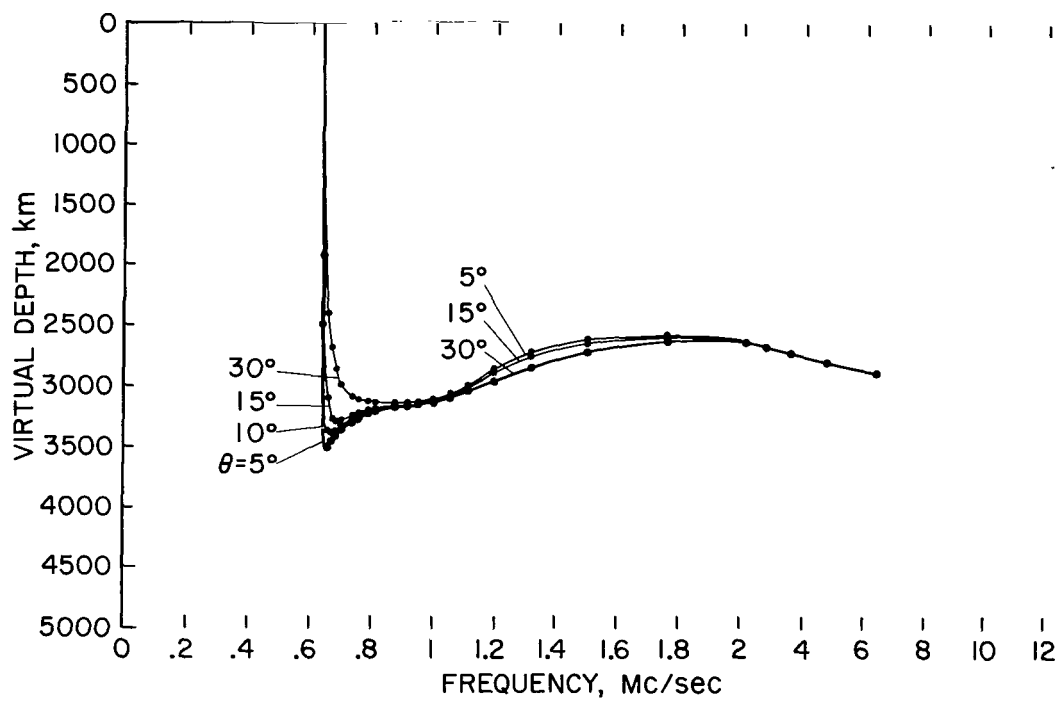


Figure 20.- Computed ordinary traces for high f_n and high f_h model profiles for $\theta = 5^\circ, 10^\circ, 15^\circ, 30^\circ$.

POSTMASTER: If Undeliverable (Section 158
Postal Manual) Do Not Return

"The aeronautical and space activities of the United States shall be conducted so as to contribute . . . to the expansion of human knowledge of phenomena in the atmosphere and space. The Administration shall provide for the widest practicable and appropriate dissemination of information concerning its activities and the results thereof."

— NATIONAL AERONAUTICS AND SPACE ACT OF 1958

NASA SCIENTIFIC AND TECHNICAL PUBLICATIONS

TECHNICAL REPORTS: Scientific and technical information considered important, complete, and a lasting contribution to existing knowledge.

TECHNICAL NOTES: Information less broad in scope but nevertheless of importance as a contribution to existing knowledge.

TECHNICAL MEMORANDUMS: Information receiving limited distribution because of preliminary data, security classification, or other reasons.

CONTRACTOR REPORTS: Scientific and technical information generated under a NASA contract or grant and considered an important contribution to existing knowledge.

TECHNICAL TRANSLATIONS: Information published in a foreign language considered to merit NASA distribution in English.

SPECIAL PUBLICATIONS: Information derived from or of value to NASA activities. Publications include conference proceedings, monographs, data compilations, handbooks, sourcebooks, and special bibliographies.

TECHNOLOGY UTILIZATION PUBLICATIONS: Information on technology used by NASA that may be of particular interest in commercial and other non-aerospace applications. Publications include Tech Briefs, Technology Utilization Reports and Notes, and Technology Surveys.

Details on the availability of these publications may be obtained from:

SCIENTIFIC AND TECHNICAL INFORMATION DIVISION
NATIONAL AERONAUTICS AND SPACE ADMINISTRATION
Washington, D.C. 20546